



HAL
open science

Embedding hexanuclear tantalum bromide cluster Ta₆Br₁₂ into SiO₂ nanoparticles by reverse microemulsion method

W. Chen, M. Wilmet, T.G. Truong, N. Dumait, Stéphane Cordier, Y. Matsui,
T. Hara, T. Takei, N. Saito, T.K.N. Nguyen, et al.

► To cite this version:

W. Chen, M. Wilmet, T.G. Truong, N. Dumait, Stéphane Cordier, et al.. Embedding hexanuclear tantalum bromide cluster Ta₆Br₁₂ into SiO₂ nanoparticles by reverse microemulsion method. *Heliyon*, 2018, 4 (6), pp.e00654. 10.1016/j.heliyon.2018.e00654 . hal-01835017

HAL Id: hal-01835017

<https://univ-rennes.hal.science/hal-01835017>

Submitted on 17 Jul 2019

HAL is a multi-disciplinary open access archive for the deposit and dissemination of scientific research documents, whether they are published or not. The documents may come from teaching and research institutions in France or abroad, or from public or private research centers.

L'archive ouverte pluridisciplinaire **HAL**, est destinée au dépôt et à la diffusion de documents scientifiques de niveau recherche, publiés ou non, émanant des établissements d'enseignement et de recherche français ou étrangers, des laboratoires publics ou privés.



Distributed under a Creative Commons Attribution - NonCommercial - NoDerivatives 4.0
International License

Received:
21 January 2018
Revised:
19 April 2018
Accepted:
7 June 2018

Cite as: Wanghui Chen,
Maxence Wilmet,
Thai Giang Truong,
Noée Dumait,
Stéphane Cordier,
Yoshio Matsui, Toru Hara,
Toshiaki Takei, Norio Saito,
Thi Kim Ngan Nguyen,
Takeo Ohsawa, Naoki Ohashi,
Tetsuo Uchikoshi,
Fabien Grasset. Embedding
hexanuclear tantalum bromide
cluster $\{\text{Ta}_6\text{Br}_{12}\}$ into SiO_2
nanoparticles by reverse
microemulsion method.
Heliyon 4 (2018) e00654.
doi: [10.1016/j.heliyon.2018.e00654](https://doi.org/10.1016/j.heliyon.2018.e00654)



Embedding hexanuclear tantalum bromide cluster $\{\text{Ta}_6\text{Br}_{12}\}$ into SiO_2 nanoparticles by reverse microemulsion method

Wanghui Chen^{a,d,*}, Maxence Wilmet^{a,b}, Thai Giang Truong^b, Noée Dumait^b, Stéphane Cordier^b, Yoshio Matsui^d, Toru Hara^e, Toshiaki Takei^f, Norio Saito^{a,d}, Thi Kim Ngan Nguyen^{a,d}, Takeo Ohsawa^{c,d}, Naoki Ohashi^{a,c,d}, Tetsuo Uchikoshi^{a,d}, Fabien Grasset^{a,d,*}

^a CNRS-Saint Gobain, UMI 3629, Laboratory for Innovative Key Materials and Structures (LINK), National Institute of Material Science, 1-1 Namiki, Tsukuba, Ibaraki, 305-0044, Japan

^b Univ Rennes, CNRS, ISCR (Institut des Sciences Chimiques de Rennes) – UMR 6226, F-35000 Rennes, France

^c NIMS-Saint-Gobain Center of Excellence for Advanced Materials, National Institute of Material Science, 1-1 Namiki, Tsukuba, Ibaraki, 305-0044, Japan

^d Research Center for Functional Materials (RCFM), National Institute for Materials Science, 1-1 Namiki, Tsukuba, Ibaraki, 305-0044, Japan

^e Research Center for Structural Materials, National Institute for Materials Science, 1-2-1 Sengen, Tsukuba, Ibaraki, 305-0047, Japan

^f Research Network and Facility Services Division, National Institute for Materials Science, 1-1 Namiki, Tsukuba, Ibaraki, 305-0044, Japan

* Corresponding authors.

E-mail addresses: CHEN.Wanghui@nims.go.jp (W. Chen), fabien.grasset@univ-rennes1.fr (F. Grasset).

Abstract

Hexanuclear tantalum bromide cluster units $[\{\text{Ta}_6\text{Br}_{12}^i\}\text{L}_6^a]$ (i = inner, a = apical, L = ligand OH or H_2O) are embedded into SiO_2 nanoparticles by a reverse microemulsion (RM) based method. $[\{\text{Ta}_6\text{Br}_{12}^i\}\text{Br}_2^a (\text{H}_2\text{O})_4^a] \cdot n\text{H}_2\text{O}$ (noted TBH) and tetraethyl orthosilicate (TEOS) are used as the starting cluster compound and the precursor of SiO_2 , respectively. The RM system in this study consists of the

n-heptane (oil phase), Brij L4 (surfactants), ethanol, TEOS, ammonia solution and TBH aqueous sol. The size and morphology of the product namely {Ta₆Br₁₂}@SiO₂ nanoparticles are analyzed by HAADF-STEM and EDS mappings. The presence and integrity of {Ta₆Br₁₂} in the SiO₂ nanoparticles are evidenced by EDS mapping, ICP-OES/IC and XPS analysis. The optical properties of {Ta₆Br₁₂}@SiO₂ nanoparticles are analyzed by diffuse reflectance UV-vis spectroscopy, further evidencing the integrity of the embedded {Ta₆Br₁₂} and revealing their oxidation state. Both {Ta₆Br₁₂}²⁺ and {Ta₆Br₁₂}³⁺ are found in SiO₂ nanoparticles, but the latter is much more stable than the former. The by-products in this RM-based synthesis, as well as their related factors, are also discussed.

Keywords: Materials chemistry, Materials science, Nanotechnology

1. Introduction

Over the past several decades, hexanuclear tantalum bromides have attracted considerable attention, in particular as a commercial tool for the phase determination of large biological assemblies by X-ray crystallography and as radiographic contrast agents [1, 2, 3, 4]. More recently, they have been proposed as efficient UV-NIR blockers for the potential application in saving energy window technology [5, 6]. Most hexanuclear tantalum bromides possess the cluster cores of {Ta₆Br₁₂}, which consists of an octahedral Ta₆ atom cluster and the 12 inner Br ligands bridging over all the 12 Ta-Ta bonds [7]. The oxidation state of {Ta₆Br₁₂} can be either 2+, 3+ or 4+, corresponding to 16, 15, and 14 valence electrons involved in its Ta₆ atom clusters, respectively [8, 9]. In most cases, 6 apical positions of Ta₆ atom cluster are further terminated by 6 ligands L (*e.g.*, Br, Cl, H₂O). These ligands are called “apical ligands” to distinguish them from the 12 inner Br ligands of {Ta₆Br₁₂}. Fig. 1 shows a typical geometry of cluster unit, as the combination of {Ta₆Br₁₂} cluster core and its apical ligands, which can be represented as the formula of [{Ta₆Br₁₂ⁱ}^{x+}L₆^a] (i = inner, a = apical, x = oxidation state 2, 3, or 4, L = ligand). The preparation of hexanuclear tantalum bromides relies on solid-state reactions performing at high temperature, while the {Ta₆Br₁₂} cluster cores in those products are fixed in extended arrays [7, 10]. For instance, reducing TaBr₅ by Ta (or other reductant metals) produces Ta₆Br₁₅ compounds, where the contained {Ta₆Br₁₂}³⁺ cluster cores connect with adjacent ones by sharing their apical Br ligands [7, 11]. A₄Ta₆Br₁₈ (A = alkali metal) are prepared by reducing TaBr₅ in the presence of ABr₅ [12, 13]. These ternary compounds are built up on the densely packed [{Ta₆Br₁₂ⁱ}Br₆^a]⁴⁺ cluster units (*i. e.*, {Ta₆Br₁₂}²⁺ terminated by 6 apical Br ligands), whose charge is counter balanced by alkali metal cations A [9]. Dissolving the solid-state hexanuclear

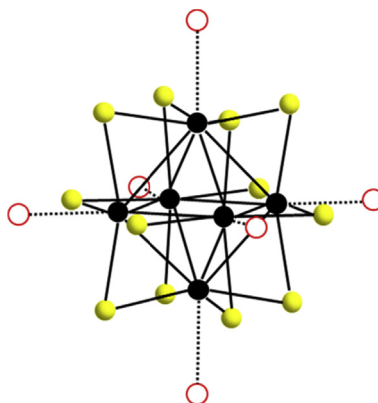


Fig. 1. Structures of an octahedral $\{Ta_6Br_{12}\}$ cluster core terminated by six axial ligands L; the black, yellow, and red spheres represent Ta atoms, edge-bridging Br anions, and terminal-ligands L, respectively.

tantalum bromides products solvated $\{Ta_6Br_{12}\}$ species, as solvent molecules lie in apical positions to form $[\{Ta_6Br_{12}^i\}Br_n^a S_{6-n}^a]^{x-n}$ ($S = \text{solvent}$; $x = 2, 3, 4$; $0 \leq n \leq 6$; $n \neq x$) cluster units [7, 14]. These cluster units are charged and act like ion, and obviously, $\{Ta_6Br_{12}\}$ cluster cores in this case are liberated and attain discrete distribution in solvent [15]. The discrete $\{Ta_6Br_{12}\}$ species are highly interesting because of their ultra-small size (*ca.* 1 nm) and the distinct electronic structure brought by the coexistence of metal-metal and covalent bonds, while they also bear the starting point of various solution based chemical/physical reactions to obtain various kinds of $[\{Ta_6Br_{12}^i\}L_6^a]$ derivatives [7, 10, 16, 17, 18, 19]. Moreover, the electronic structure of discrete $\{Ta_6Br_{12}\}$ species endows their variable optical property, depending on both the oxidation state of $\{Ta_6Br_{12}\}$ (2+, 3+ or 4+) and the properties of apical ligands—thus they can be used as the dye for transparent optical devices [5, 6, 20, 21, 22]. Meanwhile, the ion-like behaviors and ultra-small size of the discrete $\{Ta_6Br_{12}\}$ species can facilitate their homogeneous distribution in matrix and minimize the decreasing on transparency. However, to the best of our knowledge, routine method to embed the discrete $\{Ta_6Br_{12}\}$ species into inorganic matrix has not been established yet.

Reverse microemulsion (RM) is an isotropic and dynamically stable system consisting of oil, water, surfactants and sometimes co-surfactants. The water phase in RM system is well confined to uniform and nanosized swollen micelles (<100 nm), and thus it has been frequently used as the “nanoreactors” for the aqueous mediated reactions. Especially taking the advantage of the uniform size of nanoreactors, monodisperse nanoparticles can be produced in the RM based synthetic process [23, 24, 25]. This process is also efficient to combine two or more kinds of substances into nanocomposite with complex architecture

and to embed ultra-small particles into nanosized matrix, though for the latter it seems so far only the synthesis of the SiO₂-based nanocomposites have been well documented [26, 27, 28, 29, 30, 31, 32]. To prepare the so-called functionalized SiO₂ nanoparticles, silicon alkoxide (Si(OR)₄) is usually used as the precursor. Accordingly, the pH of the water phase of RM system is adjusted to over 11 to facilitate the hydrolysis and condensation over Si(OR)₄ [24]. The substances expected to be embedded into SiO₂ can either be pre-synthesized or be synthesized in situ in RM system. In the former case, the substances which possess hydrophilic surface end up to the nanoreactors after they dispersed in the RM system and are subsequently immobilized on the on-going condensing networks of ≡Si–O–Si≡. Even the substances with hydrophobic surface can also be embedded, relying on the “ligand exchanging” process with partially hydrolyzed Si(OR)₄ [33, 34]. In the latter case, the reaction become relative more complicated, as considerable attention should be devoted to the compatibility between the formation rates of the nanoparticles and of SiO₂ matrix [28]. To date, several nanocomposites like Au@SiO₂, Ag/Pd@SiO₂, CdSe@SiO₂, ZnFe₂O₄@SiO₂, Fe₃O₄@SiO₂, CeO₂@SiO₂, MoO₃@SiO₂, Ru(bpy)₃²⁺@SiO₂, etc. have been successfully prepared [35, 36, 37, 38, 39]. Most recently, the SiO₂-based nanocomposites consisting of Mo₆ and Re₆ clusters have also been successfully prepared [40, 41, 42, 43, 44]. It was demonstrated that these hexanuclear metal halide cluster units can maintain their discrete distribution in SiO₂ nanoparticles and show considerably high stability [41].

Based on the previous works, the present study is proposed to synthesize the SiO₂ nanoparticles functionalized by discrete {Ta₆Br₁₂} species (noted {Ta₆Br₁₂}@SiO₂) by RM based process. The objectives consisted are to find the conditions of a controllable and direct dispersion of a large amount of discrete {Ta₆Br₁₂} species into the nanosized SiO₂ matrix. So far, it is the first report on this topic. The advantages of SiO₂ matrix are evidenced for biotechnology and saving energy applications due to a low toxicity, high stability, easy functionalization and high transparency. Although the RM based synthesis for functionalized SiO₂ nanoparticles has been well established, there is a specific challenge to obtain the expected products. Indeed, the pH of the water phase in RM system should be over 11 to grantee the considerable formation rate of SiO₂, but the discrete {Ta₆Br₁₂} species show much higher reactivity than other metal cluster species in basic aqueous solution, generating the precipitations of [{Ta₆Br₁₂ⁱ}(OH)_x^a·(H₂O)_{6-x}]^a·nH₂O (x = 2, 3, 4) [45]. Even worse, both the hydrolysis and oxidation of {Ta₆Br₁₂} will be accelerated in the presence of OH[−], resulting in the breaking down of Ta₆Br₁₂ structural edifice and the formation of tantalum oxides. In other words, new substances will possibly generate in the RM system during the formation of SiO₂ matrix. Therefore, the products in this study are carefully characterized to prove the integrity of the encapsulated

{Ta₆Br₁₂} species, as well as their distribution, oxidation state and optical properties.

2. Experimental

2.1. Materials

Ethanol (99.5%), Ammonia solution (28 wt. %) and tetraethyl orthosilicate (TEOS, 95%) were purchased from Wako Pure Chemical Industries. *n*-heptane (98%) was purchased from Kanto Chemical Co. Nonionic surfactant Brij L4 was purchased from Sigma-Aldrich. DI water was purchased from Yamato Kagaku Co. All the chemicals were used as received without further purification. The starting compound $[(Ta_6Br_{12})Br_2(H_2O)_4] \cdot nH_2O$ (TBH) was synthesized according to a published procedure [13].

2.2. Methods

n-heptane, Brij L4, ethanol and TEOS were used as received, like oil, surfactant, co-surfactant and the precursor of SiO₂ in this RM based synthesis, respectively. TBH sol was prepared by distributing TBH powder in 1 ml DI water. To ensure its uniformity, TBH sol was first treated by ultrasonication for 15 min and then stirred for 2 hr. In different syntheses, the concentration of TBH sol (C_{TBH}) was varied from 10 to 50 mM. 3.75 ml Brij L4 and 11.75 ml *n*-heptane were mixed in a flask by vigorous stirring. Green and transparent RM formed immediately after the addition of 0.2 ml TBH solution. The stirring rate was then slowed down to 500 rpm and kept steady until the end of this synthesis. Thereafter, ethanol (volume varied from 0 to 0.6 ml in different syntheses) and 0.325 ml diluted NH₃ solution (6.5 wt. %) were added in successively with an interval of 5 min. The SiO₂ generation reaction was started by adding 0.1 ml TEOS into the RM system, and then allowed to last for 72 hr. Temperature was controlled steady at 22 °C. After the reaction, the RM system was destabilized by stirring with additional 20 ml ethanol. Dark-green particles settled down soon after the stirring stopped, leaving a colorless upper liquid. After decanting the upper liquid, the particles were collected by centrifugation (11000 rpm, 30 min) and re-dispersed in DI water by ultrasonication treatment. To obtain particles with clean surface, this washing step was repeated for 10 times. Acid washing was applied in case to remove the unexpected impurities, performed with 0.1 mM HCl solution for 3 times. Finally, the collected particles were dried in vacuum at 40 °C for 12 hr.

2.3. Instrumentation

High angle annular dark field scanning transmission electron microscopy (HAADF-STEM) images were acquired by JEM-2100F (JEOL Co.) at 200 kV. The

compositional analysis was performed by the energy dispersive X-ray spectrometer (EDS) with double wide detecting area (100 mm²) detectors equipped in a JEM-2800 (JEOL Co.) operating at 100 kV. To prepare the specimen for HAADF-STEM and EDS analysis, a small amount of RM containing the resulting {Ta₆Br₁₂}@SiO₂ nanoparticles was placed on an elastic carbon film covered Cu grid. To remove the excessive surfactants, this Cu grid was washed with dichloromethane after dry. The specimen of washed {Ta₆Br₁₂}@SiO₂ nanoparticles was prepared by placing a small amount of its water suspension on carbon film covered Cu grid, which had been treated by plasma, and completely dried in ambient condition. Powder X-ray diffraction (XRD) patterns were acquired by a D/MAX Ultima III (Rigaku Co.) diffractometer using Cu K α radiation ($\lambda = 1.5418 \text{ \AA}$) over a range of $5^\circ < 2\theta < 60^\circ$. The X-ray photoelectron spectra (XPS) were recorded using a SigmaProbe (Thermo Fisher Co.) spectrometer, with using Al-K α line (1486.6 eV) as the excitation source. XPS data treatments were carried out using the software ThermoAdvantage and the spectra energy was calibrated with the first deconvoluted C1s peak (attributed to the C–C bonding) rescaled at 284.8 eV. IR spectra were collected in the 4000–400 cm^{−1} range by a Nicolet TM 4700 FTIR spectrometer (Thermo Fisher Co.), by using KBr sampling technique. Diffuse reflectance UV-vis-NIR spectra were collected by an integrating sphere equipped V-7200 spectrometer (Jasco Co.). The absorbance UV-vis-NIR spectra of discrete {Ta₆Br₁₂}²⁺ and {Ta₆Br₁₂}³⁺ species were also collected with the sol of TBH in water and NaOH solution (molar ratio of OH[−]/Ta₆ = 8), respectively [45]. To confirm the molar ratio of Ta/Si and Br/Si in the resulting {Ta₆Br₁₂}@SiO₂ nanoparticles, ICP-OES (for Ta and Si) and ion chromatography (IC, for Br) analysis were performed.

3. Results

3.1. Phenomenology

Each {Ta₆Br₁₂} in the starting TBH is in the oxidation state of 2+ and terminated by 2 Br and 4 H₂O ligands, while the formed neutral cluster units [{Ta₆Br₁₂}Br₂^a(H₂O)₄^a] densely packed with a certain amount of water molecules to form crystal structure [13, 46]. As seen in Fig. 2, TBH fully dissolved in water and formed a homogeneous sol, whose characteristic emerald-green color implies the formation of [{Ta₆Br₁₂}^a(H₂O)₆]²⁺ cluster units [45]. The RM system composed of the TBH sol, Brij L4, *n*-heptane and ethanol were obtained subsequently, showing high homogeneity and transparency, as well as maintaining the emerald-green color. Due to the change of pH, this RM system immediately became dark green after the addition of ammonia solution. The addition of ammonia solution could also lead to turbidity, reflecting the generation of precipitates, while the rate and degree of turbidity strongly depended on the concentration of TBH sol (C_{TBH}). For instance, the RM system maintained high transparency when C_{TBH} = 10 mM, whereas it

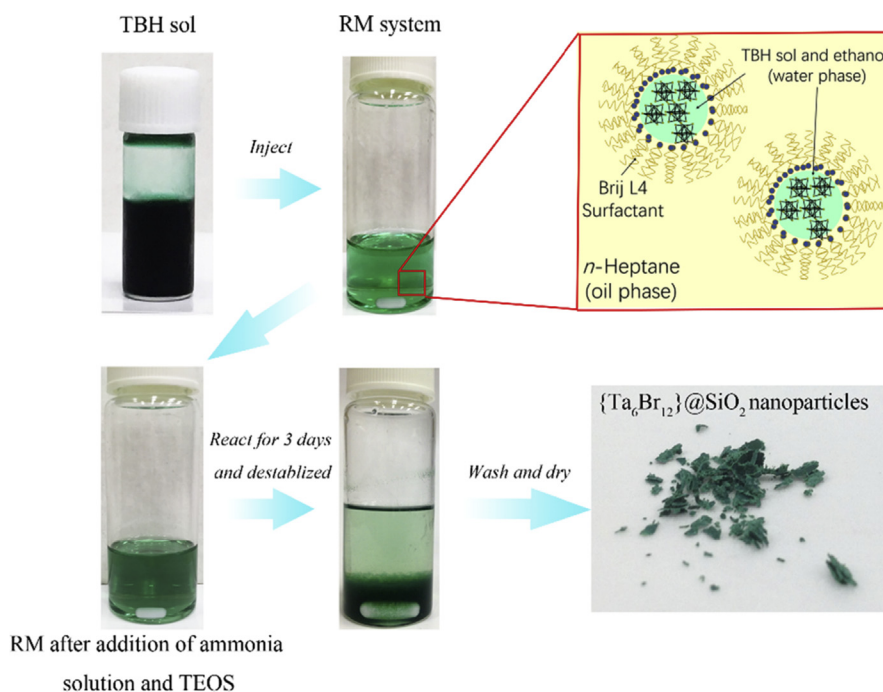


Fig. 2. Digital photographs of the RM system in different stages of the synthesis and the finally produced $\{Ta_6Br_{12}\}@SiO_2$ nanoparticles.

became turbid in *ca.* 5 min if C_{TBH} increased to 30 mM. After a sufficient reaction time for SiO_2 formation (3 days), this RM system was destabilized by stirring with excessive ethanol. Dark green particles settled down as soon as the stirring stopped, leaving colorless supernatant. After washing and drying steps, dark-green powder was obtained as the final product.

3.2. Morphology and size

Fig. 3a shows typical HAADF-STEM images of the unwashed $\{Ta_6Br_{12}\}@SiO_2$ nanoparticles. Thanks to the well confined water phase, the formed SiO_2 matrix was controlled to *ca.* 50 nm in size and showed uniform spherical shape. Both the embedded and nonembedded tantalum compounds can be found—the former consists an aggregate core centered in each $\{Ta_6Br_{12}\}@SiO_2$ nanoparticles (blue sphere in Fig. 3b) and also the discrete ultra-small (*ca.* 1 nm) particles in SiO_2 matrix (red spheres in Fig. 3b), the latter consists of the ultra-small particles agglomerating on the outer surface of SiO_2 . Fig. 3b indicates the nonembedded tantalum compounds were mostly removed in the washing steps, leaving a clean surface of SiO_2 matrix, while the embedded tantalum compounds seem not to be affected by washing, like that for Mo_6 clusters in the previous study [41]. Fig. 4 shows the HAADF-STEM image of the washed $\{Ta_6Br_{12}\}@SiO_2$ nanoparticles and its corresponding EDS analysis. All the peaks of Si, O, Ta and Br are shown on the EDS spectrum

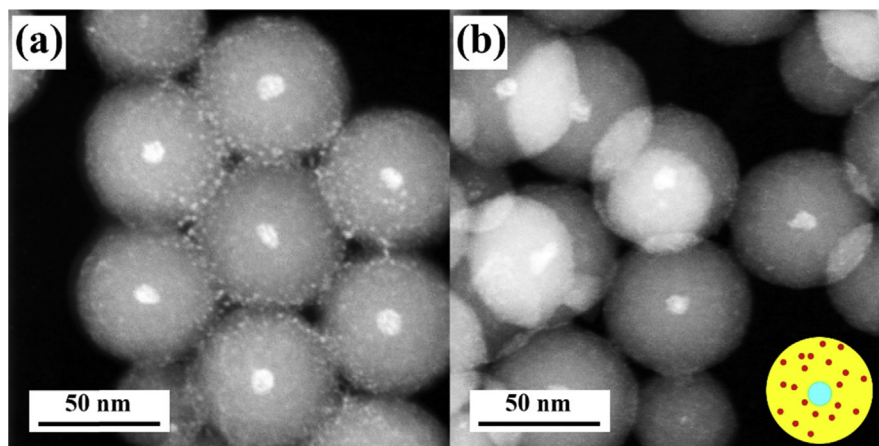


Fig. 3. HAADF-STEM images of $\{Ta_6Br_{12}\}@SiO_2$ nanoparticles ($C_{TBH} = 10$ mM) sampled before (a) and after (b) washing step; The insert of (a) is the corresponding low magnification HAADF-STEM image, wherein the scale bar represents 200 nm; The insert of (b) demonstrates the architecture of the particles in (b), where the SiO_2 matrix, aggregate core and discrete ultra-small particles are differentiated by yellow, blue and red color, respectively.

(Fig. 4e), indicating tantalum bromides were successfully embedded into the SiO_2 nanoparticles, though it is still hard to confirm at this stage if the embedded tantalum bromides are $\{Ta_6Br_{12}\}$ species. The EDS mappings of Si, Ta and Br elements (Fig. 4b–d) are in good agreement with the morphology shown in Fig. 3b—the embedded tantalum compounds are not only rich in the aggregate core part of SiO_2 nanoparticles but also disperse thoroughly in the whole SiO_2 matrix.

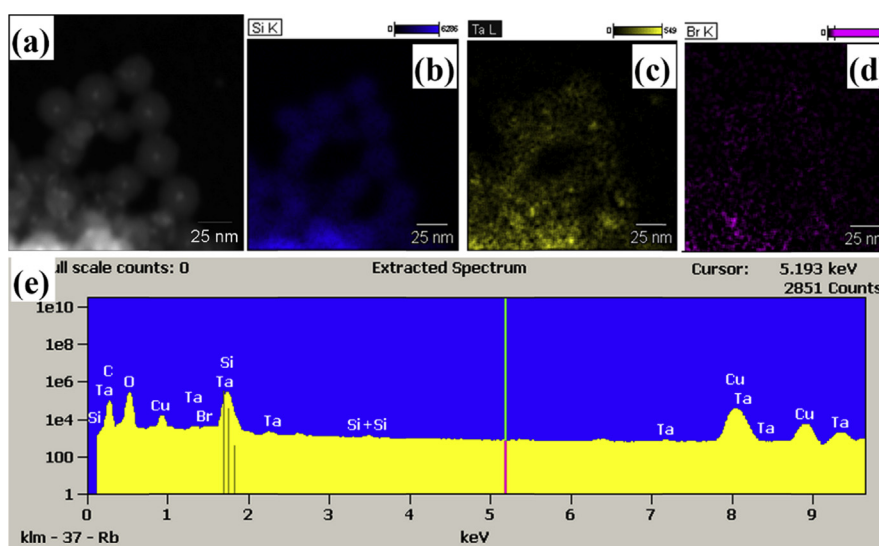


Fig. 4. HAADF-STEM image (a) of $\{Ta_6Br_{12}\}@SiO_2$ nanoparticles ($C_{TBH} = 10$ mM) and the corresponding EDS mappings indicating the distribution of Si (b) Ta (c), and Br (d) elements; (e) is the EDS spectrum of the full scale of (a).

Indicated by a series of syntheses, the amount of the embedded tantalum compounds in SiO_2 matrix strongly depended on C_{TBH} and the molar ratio of ethanol versus H_2O (noted R) in RM system. Fig. 5 shows HAADF-STEM images of the washed $\{\text{Ta}_6\text{Br}_{12}\}@ \text{SiO}_2$ nanoparticles synthesized with $C_{\text{TBH}} = 10, 20, 30,$ and 40 mM and keeping all other synthetic parameters the same. Particles in all these samples show narrow size distribution due to the advantages of RM system, despite their average size slightly decreases from 50 nm to 40 nm with increasing C_{TBH} . Moreover, increasing C_{TBH} did not vary the size of aggregate core (*ca.* 10 nm) in each particle but significantly increased the density of the ultra-small tantalum compounds in SiO_2 matrix. It is also noteworthy that the nonembedded tantalum compounds started to appear outside of SiO_2 matrix when C_{TBH} reached 40 mM (Fig. 5d). On the other hand, decreasing R in RM system was not favorable for obtaining $\{\text{Ta}_6\text{Br}_{12}\}@ \text{SiO}_2$ nanoparticles with homogeneous morphology, because it

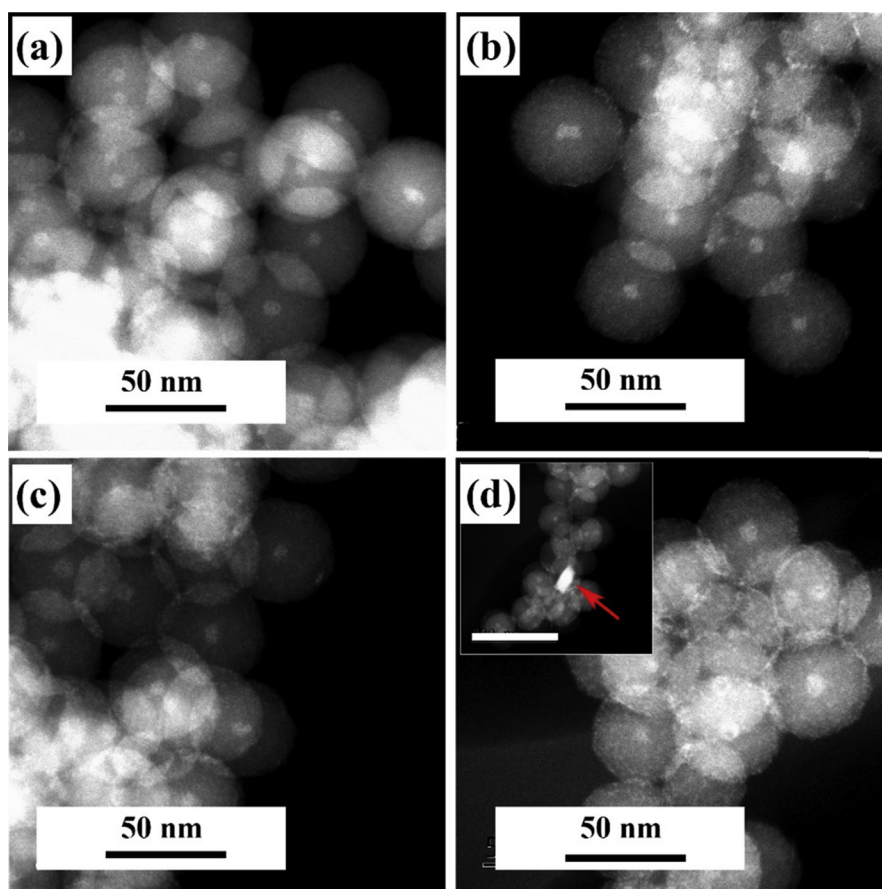


Fig. 5. HAADF-STEM images of the $\{\text{Ta}_6\text{Br}_{12}\}@ \text{SiO}_2$ nanoparticles synthesized with $C_{\text{TBH}} = 10$ mM (a), 20 mM (b), 30 mM (c) and 40 mM (d), respectively; all these samples were synthesized with $R = 0.37$ and washed for 10 times with water; the insert of (d) is the corresponding low magnification HAADF-STEM image with an arrow pointing to an irregular shaped aggregate of tantalum compounds out of SiO_2 matrix, wherein the scale bar represents 100 nm.

led to the presence of more aggregates of tantalum compounds outside the SiO₂ matrix. As seen in Fig. 6a, when R reduced to 0.24, a number of nonembedded aggregates started to appear outside of SiO₂ matrix despite the low C_{TBH} (30 mM). More representatively, when R = 0 (*i.e.*, no ethanol contained in RM system), the generated nonembedded aggregates were so large that capped on several {Ta₆Br₁₂}@SiO₂ nanoparticles (Fig. 6b). Accordingly, only a small number of tantalum compounds were embedded into the SiO₂ nanoparticles (insert of Fig. 6b). In addition, the EDS spectra in Fig. 7 demonstrates both the Ta and Br elements are contained in the irregular shaped aggregates.

3.3. X-ray diffraction analyses

Fig. 8 shows the XRD patterns of the starting TBH and the as-synthesized {Ta₆Br₁₂}@SiO₂ nanoparticles synthesized under different conditions. The XRD pattern of TBH (Fig. 8a) agrees with the pattern of Ta₆Br₁₄·8H₂O reported by Spreckelmeyer et al, reflecting the dense packing of [{Ta₆Br₁₂}Br₂(H₂O)₄] cluster units [47]. Such long-range-order structure is supposed to disappear within the dissolution of TBH and the following RM based process. As expected, no diffraction peak showing on the patterns of {Ta₆Br₁₂}@SiO₂ nanoparticles can be assigned to the characteristic peaks of TBH. On the patterns of {Ta₆Br₁₂}@SiO₂ nanoparticles synthesized with C_{TBH} = 10, 20, 30 mM (Fig. 8b–d), the broad peak maximum at 2θ = 24° is the most significant, which can be assigned to the amorphous SiO₂ matrix. Despite the sharp diffraction peak maximum at 2θ = 18° can hardly be defined at the current stage, it implies the formation of either new densely packed array of cluster units or other tantalum compounds in the {Ta₆Br₁₂}@SiO₂ nanoparticles. Further take

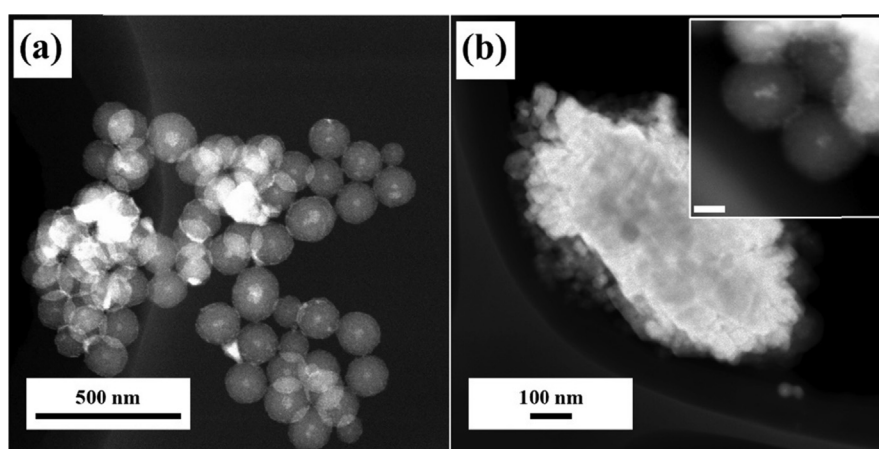


Fig. 6. HAADF-STEM images of {Ta₆Br₁₂}@SiO₂ nanoparticles synthesized with R = 0.24 (a) and 0 (b); the insert of (b) is the corresponding high magnification image with the scale bar representing 10 nm; both of these two samples were synthesized with C_{TBH} = 30 mM and washed for 10 times with water.

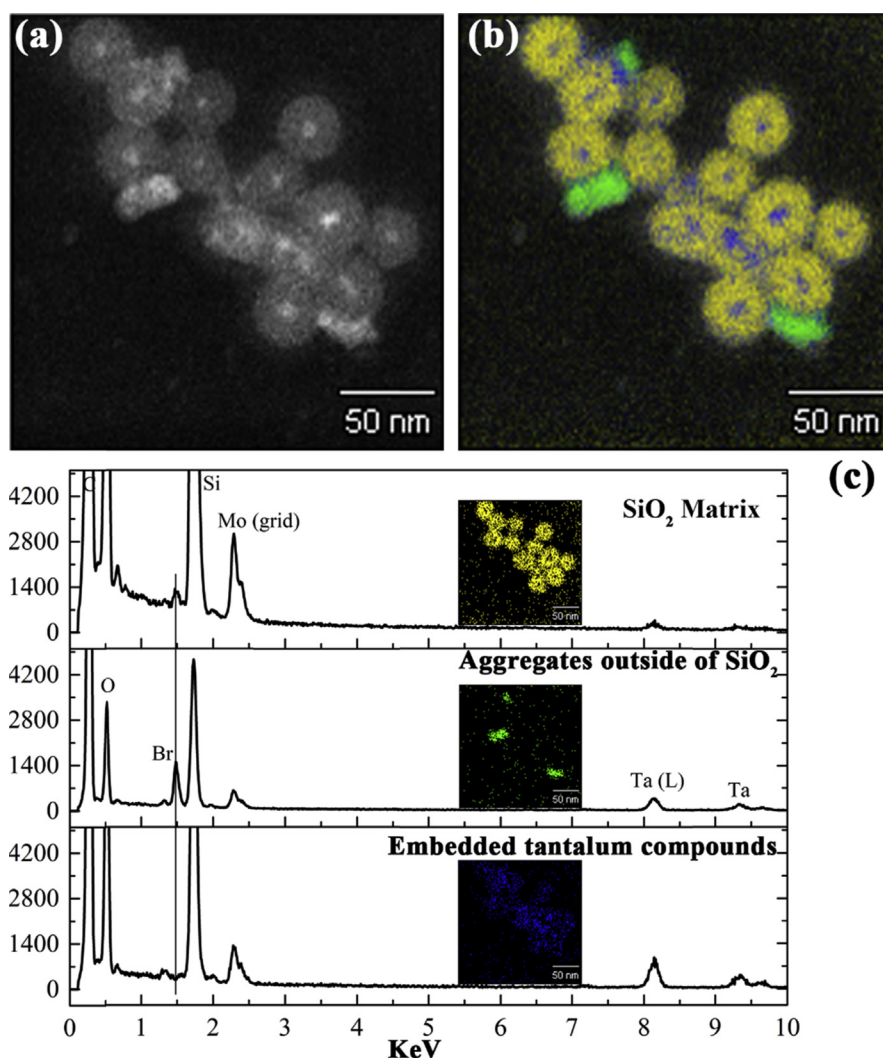


Fig. 7. HAADF-STEM image (a) and the phase mapping from the multi-variant analysis of EDS (b) of the $\{Ta_6Br_{12}\}@SiO_2$ nanoparticles synthesized with $C_{TBH} = 40$ mM, $R = 0.37$; (c) show the EDS spectrum of each phase.

account of the texture of these samples (Fig. 5a–c), the tantalum compounds acting as the aggregate cores centered in SiO_2 nanoparticles should be in crystal form, assuming that discrete $\{Ta_6Br_{12}\}$ species are not able to produce diffraction peaks because of the lack of dense packing which leads to crystal structure. Much more diffraction peaks appear on the XRD patterns when C_{TBH} increased to 40 mM (Fig. 8d) or R decreased to 0 (Fig. 8e). Obviously, these peaks can be ascribed to the promptly generated nonembedded aggregates of tantalum compounds, which presented outside of SiO_2 matrix and remained in samples after washing steps. The XRD pattern in Fig. 9 indicates the aggregates were efficiently, though not completely, removed in the acid washing steps.

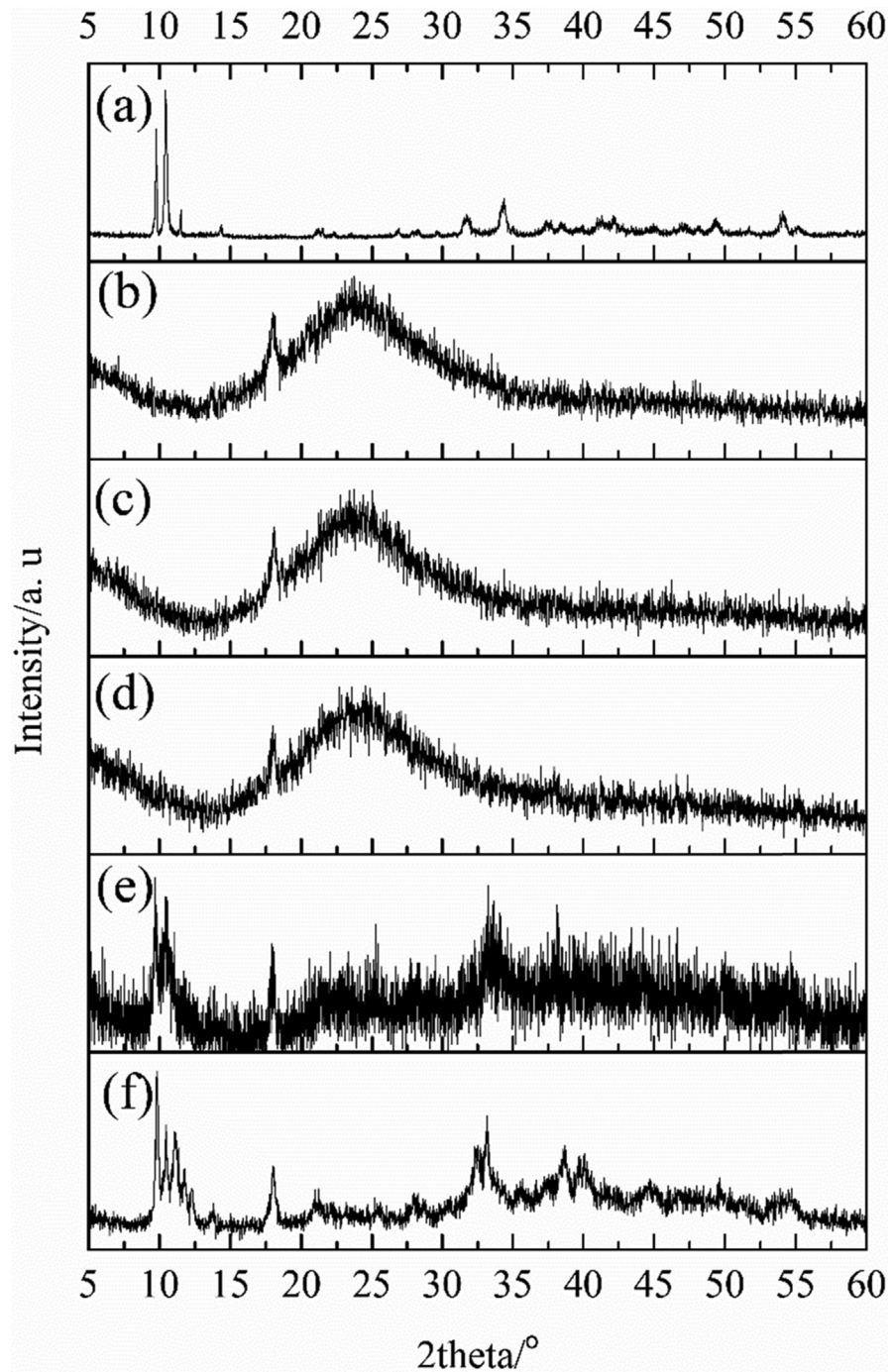


Fig. 8. XRD patterns of the starting TBH (a), $\{\text{Ta}_6\text{Br}_{12}\}@ \text{SiO}_2$ nanoparticles synthesized with $C_{\text{TBH}} = 10$, $R = 0.37$ (b), $C_{\text{TBH}} = 20$, $R = 0.37$ (c), $C_{\text{TBH}} = 30$, $R = 0.37$ (d), $C_{\text{TBH}} = 40$, $R = 0.37$ (e), and $C_{\text{TBH}} = 30$, $R = 0$ (f); all these samples were washed for 10 times with water.

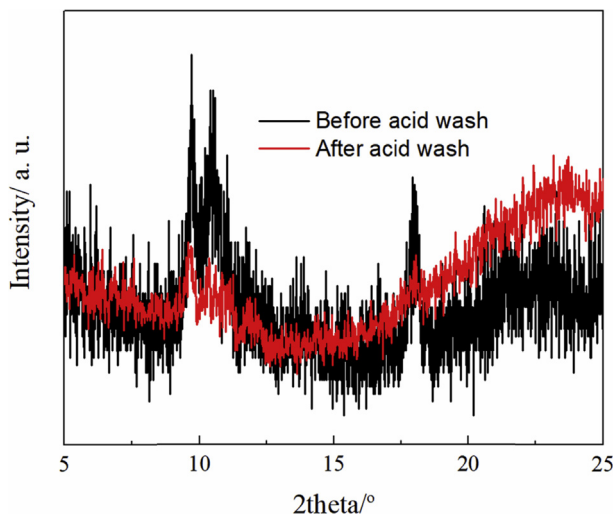


Fig. 9. XRD patterns of the $\{Ta_6Br_{12}\}@SiO_2$ nanoparticles before and after acid wash; these particles were synthesized with $C_{TBH} = 40$ mM, $R = 0$.

3.4. Chemical analysis

A series of ICP-OES/IC characterizations was carried out to determine the actual molar ratio of Ta/Si, Br/Si and Br/Ta in the as-synthesized $\{Ta_6Br_{12}\}@SiO_2$ nanoparticles. For all the washed and acid-washed samples, the molar ratio of Ta/Si and Br/Si were estimated and plotted versus C_{TBH} in Fig. 10a. The corresponding theoretical ratio Ta/Si and Br/Si in each sample was calculated by assuming that all the TEOS has condensed to form SiO_2 and that all the introduced $\{Ta_6Br_{12}\}$ species have been embedded in. Same as that observed for the embedding of Mo_6 metal clusters in SiO_2 nanoparticles, the result show that the amount of embedded tantalum compounds is always below its corresponding theoretical one [41]. Also shown in Fig. 10a, the deviation between the experimental and theoretical values of Ta/Si

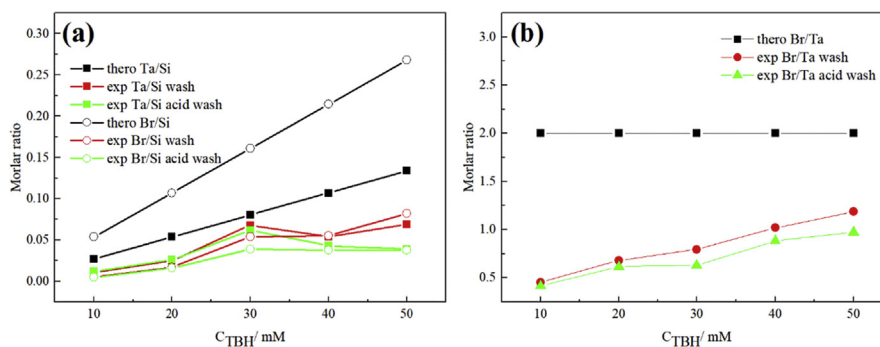


Fig. 10. (a) molar ratios of Ta/Si (full symbols) and Br/Si (empty symbols) obtained by theoretical calculations (black), ICP-OES/IC measurements of water washed (red) and 0.1 mM HCl washed (green) $\{Ta_6Br_{12}\}@SiO_2$ nanoparticles, depending on the C_{TBH} ; the molar ratio of Br/Ta in each sample is calculated and plotted versus C_{TBH} in (b).

and Br/Si increase as increasing C_{TBH} or after acid-washing process. This observation indicates that the efficiency of the encapsulation of the tantalum compounds inside the SiO_2 nanoparticles is limited by their solubility in the SiO_2 . As seen, the molar ratio of Ta/Si increases when $C_{\text{TBH}} < 30$ mM and there is no significant difference between the washed and acid-washed samples in this range of C_{TBH} . On contrary when $C_{\text{TBH}} > 30$ mM, the molar ratios seem to reach a plateau and there is no increasing of the Ta/Si along with increasing C_{TBH} . Meanwhile, the Ta/Si ratios of the acid-washed samples are much lower than their corresponding washed sample. Such difference is possibly due to the removing of nonembedded clusters in washing step. The trend of Br/Si ratio is close to that of Ta/Si, except the large difference between that of the washed and acid-washed sample starts to appear when $C_{\text{TBH}} = 30$ mM. Moreover, the ratio of Br/Ta in each sample, which is also plotted versus C_{TBH} in Fig. 10b, reflects the apparent chemical composition of the embedded tantalum compounds. The theoretical value of 2 for the Br/Ta molar ratio is confirmed as all the embedded tantalum compounds are $[\{\text{Ta}_6\text{Br}_{12}^i\}\text{L}_6^a]$ ($\text{L} = \text{H}_2\text{O}$ or OH), and all the free Br^- in SiO_2 matrix (*i. e.*, the dissociated apical Br ligands, generated within the dissolution of TBH) have been removed in the washing steps. Unfortunately, the Br/Ta ratios in all these samples were much lower than 2, though it increased with increasing of C_{TBH} . This result suggests a considerable portion of $\{\text{Ta}_6\text{Br}_{12}\}$ species lost their integrity in the embedding process, followed by the removing of the generated free Br^- anions from SiO_2 nanoparticles (in washing steps).

To further study the chemical composition of the embedded tantalum compounds, the Br environment in the $\{\text{Ta}_6\text{Br}_{12}\}@\text{SiO}_2$ nanoparticles was analyzed by XPS characterization. Fig. 11 and Table 1 summarize the acquired Br 3p core-level spectra and peak binding energies, respectively, of both the starting TBH and $\{\text{Ta}_6\text{Br}_{12}\}@\text{SiO}_2$ nanoparticles. As seen, both Br 3p spectra of these two samples are found in the region of 178–194 eV, splitting to two lines of Br 3p_{1/2} and Br 3p_{3/2}. Deconvoluting the Br 3p_{1/2} and Br 3p_{3/2} energies of TBH gave two sets of spin-orbit doublets (marked by blue and green in Fig. 11a), reflecting the presence of two Br environments in TBH, noted Br₁ and Br₂ in Table 1, respectively. The area ratio of the higher energy to the lower energy doublet (*i. e.*, $[\text{Br}_1(3\text{p}_{1/2}) + \text{Br}_1(3\text{p}_{3/2})] : [\text{Br}_2(3\text{p}_{1/2}) + \text{Br}_2(3\text{p}_{3/2})]$) was calculated to 6:1. Taking account of the composition of TBH, the higher energy doublet (Br₁) could be assigned to the edge-bridging Br anions, while the lower energy doublet (Br₂) could be assigned to the apical Br ligands. These assignments are consistent with the previous study carried out by Best et al, where the environments of Br₁ and Br₂ were unconventionally denoted as Br_b and Br_t, respectively [48]. Regarding the Br 3p spectrum of $\{\text{Ta}_6\text{Br}_{12}\}@\text{SiO}_2$ nanoparticles, it was also deconvoluted to two sets of doublets (Fig. 11b). Table 1 reveals the higher energy doublet of $\{\text{Ta}_6\text{Br}_{12}\}@\text{SiO}_2$ nanoparticles was in good agreement with that of TBH, in terms of both binding energy and

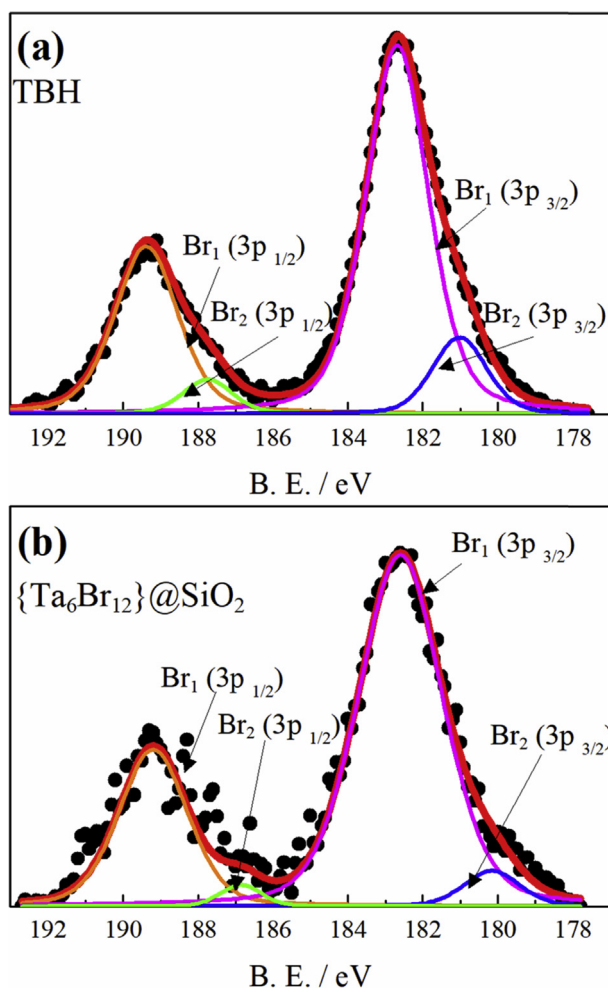


Fig. 11. Br 3p binding energy spectra of TBH (a) and $\{\text{Ta}_6\text{Br}_{12}\}@/\text{SiO}_2$ nanoparticles (b); the experimental and fitting curves are plotted in black and red, respectively; the two sets of Br 3p_{1/2}, _{3/2} doublet that from deconvolution are differentiated by blue and green colors.

full width at half maximum (FWHM). Therefore, the consistence of the Br₁ environment in the starting TBH and $\{\text{Ta}_6\text{Br}_{12}\}@/\text{SiO}_2$ nanoparticles was evidenced, and thus demonstrating the integrity of $\text{Ta}_6\text{Br}_{12}$ structural edifice maintained in the as-synthesized $\{\text{Ta}_6\text{Br}_{12}\}@/\text{SiO}_2$ nanoparticles. It should be point out that this conclusion can only apply to the embedded tantalum compounds near the out surface of SiO_2 matrix, as the tantalum compound in the aggregate core part of $\{\text{Ta}_6\text{Br}_{12}\}@/\text{SiO}_2$ nanoparticles is ca. 20 nm far from the out surface but the analysis depth of the current Al-K α XPS characterizations is ca. 5 nm. On another hand, the lower energy doublet (Br₂) of $\{\text{Ta}_6\text{Br}_{12}\}@/\text{SiO}_2$ nanoparticles shows a significant red shift with respect to that of TBH, and the area ratio of Br₁: Br₂ drastically increased to 14:1 (or 12:0.85). Hence, the Br₂ environment of $\{\text{Ta}_6\text{Br}_{12}\}@/\text{SiO}_2$ nanoparticles could not be seen as from the apical Br ligands any longer, and is possibly based on the free Br⁻ anions remaining in SiO_2 matrix after the washing steps.

Table 1. X-ray photoelectron spectra of Br 3p^{a)} in TBH and {Ta₆Br₁₂}@SiO₂ nanoparticles.

Sample	Br ₁ ^{b)}		Br ₂ ^{c)}	
	3p _{1/2}	3p _{3/2}	3p _{1/2}	3p _{3/2}
TBH	189.4 (2.0)	182.7 (2.0)	187.8 (1.6)	181.0 (1.7)
{Ta ₆ Br ₁₂ }@SiO ₂	189.2 (1.9)	182.6 (2.2)	186.8 (1.8)	180.1 (1.9)

^{a)} Binding energies in eV, with FWHM values given in parentheses.

^{b)} Br₁ represents the Br 3p_{1/2}, 3/2 doublets with higher binding energy.

^{c)} Br₂ represents the Br 3p_{1/2}, 3/2 doublets with lower binding energy.

3.5. Optical properties

Fig. 12a plots the diffuse reflectance UV-vis spectra of {Ta₆Br₁₂}@SiO₂ nanoparticles synthesized with different C_{TBH} (spectrum a-e), and the absorption spectra of discrete {Ta₆Br₁₂}²⁺ and {Ta₆Br₁₂}³⁺ species in aqueous solution are shown in

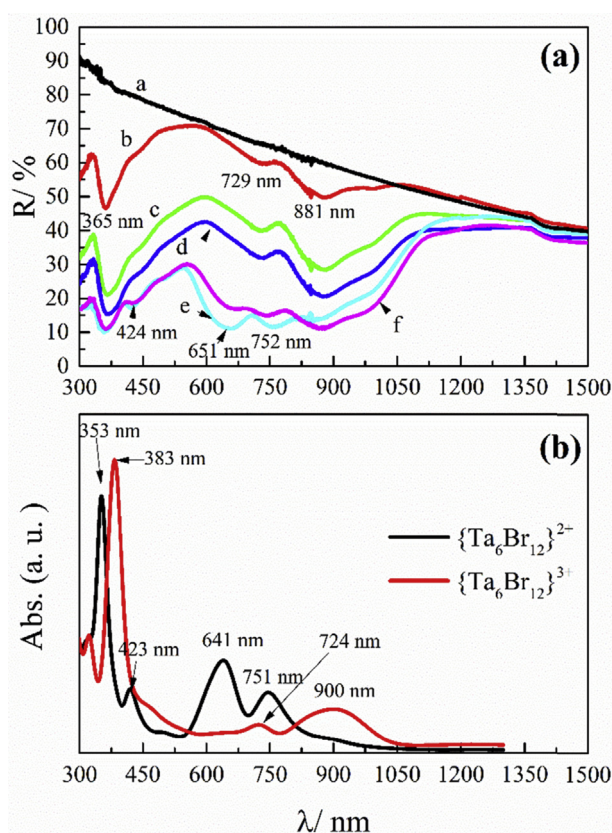


Fig. 12. (a) the diffuse reflectance UV-vis-NIR spectra of the {Ta₆Br₁₂}@SiO₂ nanoparticles synthesized with C_{TBH} = 0 mM (spectrum a), 10 mM (spectrum b), 20 mM (spectrum c), 30 mM (spectrum d) and 40 mM (spectrum e); spectrum f corresponds to the sample synthesized with C_{TBH} = 40 mM and aged for 2 months; (b) the UV-vis absorption spectra of aqueous solution containing discrete {Ta₆Br₁₂}²⁺ and {Ta₆Br₁₂}³⁺ species.

Fig. 12b for reference. To eliminate the effect of the impurity of tantalum compound aggregates formed outside SiO₂ nanoparticles on the spectrum, the {Ta₆Br₁₂}@SiO₂ nanoparticles synthesized with C_{TBH} = 40 mM were pretreated with 0.1 mM HCl solution. As seen, there is no significant absorption peak appears on the reflectance spectrum of pure SiO₂ nanoparticles (*i.e.*, synthesized with C_{TBH} = 0, spectrum a) within the wavelength range from 300 to 1500 nm. Functionalizing these SiO₂ nanoparticles with discrete {Ta₆Br₁₂} species (C_{TBH} ≤ 30 mM, spectrum b, c, and d) introduced several absorption bands in UV-vis-NIR region, which were maximum at the wavelength of 365, 729, and 881 nm respectively. The intensities of absorption bands increased with increasing C_{TBH}, keeping their position consistent with each other. Moreover, all the absorption peaks of these {Ta₆Br₁₂}@SiO₂ nanoparticles show one to one correspondence with those of discrete {Ta₆Br₁₂}³⁺ species in aqueous solution, maximum at the wavelength of 383, 724 and 900 nm. Despite the slight shifts between the absorption of {Ta₆Br₁₂} species in SiO₂ matrix and that of {Ta₆Br₁₂}³⁺ species in aqueous solution, this correspondence indicates the 3+ oxidation state of the embedded {Ta₆Br₁₂} [7, 8, 20, 21, 22, 49]. The {Ta₆Br₁₂}²⁺ only presented in the {Ta₆Br₁₂}@SiO₂ nanoparticles synthesized with C_{TBH} = 40 mM (spectrum e), indicated by three new absorptions maximum at the wavelength of 424, 651, and 752 nm, which show one to one correspondence with the characteristic absorption of {Ta₆Br₁₂}²⁺ species in aqueous solution (maximum at the wavelength of 423, 641 and 751 nm). However, the spectrum f in Fig. 12a, corresponding to the {Ta₆Br₁₂}@SiO₂ nanoparticles synthesized with C_{TBH} = 40 mM and had been stored for 2 months, suggests the discrete {Ta₆Br₁₂}²⁺ species in SiO₂ matrix were much more unstable, as all the characteristic absorptions of {Ta₆Br₁₂}²⁺ species decreased along with the increasing absorption at the wavelength of 881 nm.

4. Discussion

Two reactions took place in the RM based process: i) the reaction of [{Ta₆Br₁₂}ⁱ(H₂O)₆]²⁺ cluster units with NH₄OH and ii) the formation of SiO₂ nanoparticles. Unlike the well documented latter one, the former reaction can be considerably complicated. According to previous studies on the base titration of [{Ta₆Br₁₂}ⁱ(H₂O)₆]²⁺ cluster units in aqueous solution, the reactions of precipitation (generating [{Ta₆Br₁₂}ⁱ(OH)_x(H₂O)_{6-x}]·nH₂O (x = 2, 3, 4), oxidation (generating {Ta₆Br₁₂}^{3/4+} species) and decomposition of Ta₆Br₁₂ structural edifice (generating TaBr_xO_y compound) may take place [45]. Therefore, the distribution, oxidation state and integrity of the embedded {Ta₆Br₁₂} species in SiO₂ matrix should be carefully discussed. Indeed, we observed four tantalum compound related phases by HAADF-STEM analysis, as the (1) ultra-small particles in SiO₂ shells, (2) aggregate cores centered in SiO₂ nanoparticles, (3) ultra-small particles adhering on the surface of SiO₂ shells, and (4) irregular shaped aggregates outside of SiO₂ matrix.

According to the previous characterizations, properties of phase (1) can be summarized as i) consisting of the discretely dispersed tantalum compounds, the size of which is comparable with that of a single cluster (by HAADF-STEM and EDS mapping characterizations); ii) maintaining the integrity of $\text{Ta}_6\text{Br}_{12}$ structural edifice (by XPS characterization); iii) introducing concentrated phase (1) by using high C_{TBH} leads to the increased absorptions of $\{\text{Ta}_6\text{Br}_{12}\}@\text{SiO}_2$ (by diffuse reflectance UV-vis-NIR characterizations). Therefore, we can demonstrate that the phase (1) consists of discrete $\{\text{Ta}_6\text{Br}_{12}\}$ species embedded in SiO_2 matrix, which is also the objective product of this study. The diffuse reflectance UV-vis spectra also demonstrated that most all the embedded $\{\text{Ta}_6\text{Br}_{12}\}$ are in the oxidation state of $3+$, while the $\{\text{Ta}_6\text{Br}_{12}\}^{2+}$ could be found in the samples synthesized with high C_{TBH} but showing poor stability even in ambient condition. The transformation from $\{\text{Ta}_6\text{Br}_{12}\}^{2+}$ species (in TBH and its sol) to $\{\text{Ta}_6\text{Br}_{12}\}^{3+}$ species (in $\{\text{Ta}_6\text{Br}_{12}\}@\text{SiO}_2$ nanoparticles) was possibly due to the accelerated oxidation rate of $[\{\text{Ta}_6\text{Br}_{12}\}(\text{H}_2\text{O})_6^i]^{2+}$ cluster units in basic solution. Though this process can hardly be prevented at current stage of this study, the obtained SiO_2 nanoparticles functionalized by $\{\text{Ta}_6\text{Br}_{12}\}^{3+}$ species are still very interesting for UV-NIR blockers or other optical applications, attributed to their strong absorptions in both the UV and NIR regions [5, 6]. Furthermore, the apical ligands of the $\{\text{Ta}_6\text{Br}_{12}\}$ in phase (1) can be either H_2O or OH^- but not Br^- , as the XPS characterization revealed the apical Br dissociated within the RM based process. It is also indicated the free Br^- anions were removed to a considerable extent in washing steps, resulted in the high $\text{Br}_1:\text{Br}_2$ (12: 0.85). Therefore, by assuming the residues of Br^- in SiO_2 matrix acting as the counter anions, the structure of cluster units in phase (1) can be written as $\text{Br}_{0.85}[\{\text{Ta}_6\text{Br}_{12}^i\}^{3+}(\text{H}_2\text{O})_{3.85}(\text{OH})_{2.15}]$. In case of the $\{\text{Ta}_6\text{Br}_{12}\}^{2+}$ species, these cluster units can be written as $\text{Br}_{0.85}[\{\text{Ta}_6\text{Br}_{12}^i\}^{2+}(\text{H}_2\text{O})_{4.85}(\text{OH})_{1.15}]$. Aubert et al proposed a similar formula for the embedded Mo_6 species in SiO_2 matrix, which could be used to explain the strong interaction between cluster units matrix—hydrogen bonds formed between the apical ligands OH^- and Si-OH groups [41].

The embedded tantalum compounds also contain the phase (2)—consisting of an aggregate core in the center of each SiO_2 nanoparticle. However, these compounds cannot be seen as consisting of discrete cluster units any more, as they show a much larger size (*ca.* 10 nm) and XRD analysis suggested they possess crystal structure. Though EDS mapping indicated these cores composed by Ta and Br elements, but it is still hard to know their actual composition. The ICP-OES/IC results indicated the apparent molar ratio of Br/Ta of all the embedded tantalum compounds is lower than theoretical 2, indicating the decomposition of a proportion of $\{\text{Ta}_6\text{Br}_{12}\}$. Because phase (1) has been proved to the discrete cluster units with the molar ratio of Br/Ta slightly larger than 2, the breaking down of the $\text{Ta}_6\text{Br}_{12}$ structural edifice possibly took place within the formation of aggregate cores and

released free Br⁻ anions. Therefore, phase (2) is assigned to TaBr_xO_y compound, yielding due to the decomposition of {Ta₆Br₁₂} species.

Both the phase (3) and (4) refer to the nonembedded tantalum compounds, whereas they showed distinct texture in HAADF-STEM observation and possibly relate to different forming mechanism. The tantalum compounds in phase (3) can also be assigned to the discrete {Ta₆Br₁₂} species, as they show comparable size with those in phase (1). Further TEM observations (Fig. 13) indicated the affinity of those compounds with the surfactants Brij L4 on the out surface of SiO₂ nanoparticles. Therefore, phase (3) were possibly originated by the coordination of {Ta₆Br₁₂} species with the -OH groups of the Brij L4. Since these complexes in RM system stay between oil and aqueous phase, that this part of {Ta₆Br₁₂} species were not embedded into SiO₂ matrix but immobilized on its out surface. Indeed, phase (3) disappeared along with the removing of surfactants within washing steps. On contrary, the tantalum compounds in phase (4) show an irregular shape and much larger size—even larger than the size of SiO₂ nanoparticles under some certain synthetic conditions. The ICP-OES/IC analysis suggested that the presence of phase (4) closely relates with the saturation of tantalum compounds in SiO₂ matrix. In this study, we observed such saturation occurred when C_{TBH} reached 30 mM, and a higher C_{TBH} did not increase the amount of embedded tantalum compounds but resulted in the emerging of phase (4). Therefore, the phase (4) are possibly the promptly generated precipitates $[\{Ta_6Br_{12}\}(OH)_x(H_2O)_{6-x}] \cdot nH_2O$ ($x = 2, 3, 4$), whose size was so large that could not entirely stay inside the “nanoreactors” of RM system or further be encapsulated by SiO₂. On another hand, the molar ratio of ethanol: H₂O (R) in the RM system also acted as an important parameter, as the phase (4) promptly generated when

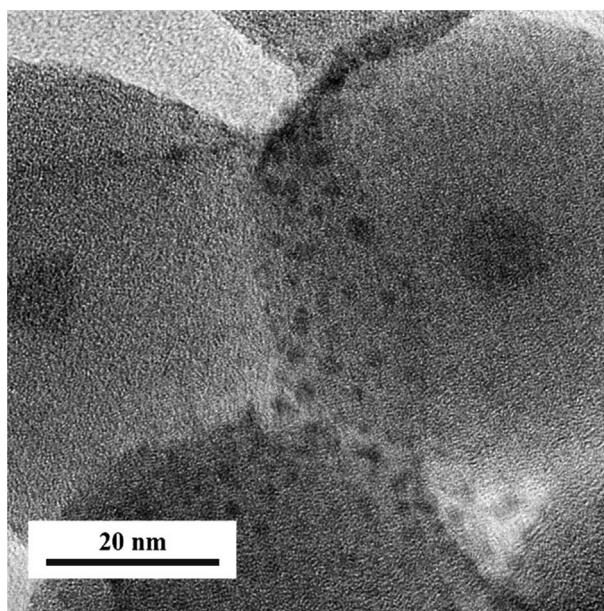


Fig. 13. TEM image of the {Ta₆Br₁₂}@SiO₂ nanoparticles sampled before washing steps.

both C_{TBH} and R was low. This phenomenon can be explained by the different behavior of $[\{\text{Ta}_6\text{Br}_{12}\}(\text{H}_2\text{O})_6^{\text{a}}]^{2+}$ cluster units in water and water-ethanol mixture. Indeed, the precipitates $[\{\text{Ta}_6\text{Br}_{12}\}(\text{OH})_x^{\text{a}}(\text{H}_2\text{O})_{6-x}^{\text{a}}] \cdot n\text{H}_2\text{O}$ can be re-dissolved by alkoxides, rendering more discrete $\{\text{Ta}_6\text{Br}_{12}\}$ species staying in basic solution [45].

5. Conclusion

In this study, we successfully embedded discrete hexanuclear tantalum bromide cluster units $[\{\text{Ta}_6\text{Br}_{12}\}\text{L}_6^{\text{a}}]$ (i = inner, a = apical, L = ligand OH or H_2O) inside SiO_2 nanoparticles by a reverse microemulsion (RM) based synthesis for the first time. The compound $[\{\text{Ta}_6\text{Br}_{12}\}\text{Br}_2^{\text{a}}(\text{H}_2\text{O})_4^{\text{a}}] \cdot n\text{H}_2\text{O}$ (TBH) was used as the starting material and the RM system was composed by *n*-heptane, Brij L4, ethanol, ammonia solution and the TBH sol. Thanks to the well confined water phase in RM system, the obtained $\{\text{Ta}_6\text{Br}_{12}\}@\text{SiO}_2$ nanoparticles showed narrow size distribution and average size of 40–50 nm. The presence of discrete $\{\text{Ta}_6\text{Br}_{12}\}$ species inside SiO_2 matrix was confirmed by HAADF-STEM and EDS mapping analyses, and XPS characterization further demonstrated their integrity. However, a series of ICP-OES/IC characterizations revealed not all the embedded tantalum compounds were discrete $\{\text{Ta}_6\text{Br}_{12}\}$ species, as a TaBr_xO_y particle with the size ca. 10 nm was found as the core in each SiO_2 nanoparticles. Formation of this kind of by-products was possibly due to the decomposition of $\text{Ta}_6\text{Br}_{12}$ structural edifice in the presence of NH_4OH . Other kind of by-products (*i.e.*, nonembedded tantalum compounds) could be removed in post-treatments or be prevented their generation by adjusting synthetic parameters. The diffuse reflectance UV-vis spectrum not only indicated the presence of discrete $\{\text{Ta}_6\text{Br}_{12}\}$ species in SiO_2 nanoparticles but also further revealed that 3+ is their stable oxidation state. Indeed, the embedded discrete $\{\text{Ta}_6\text{Br}_{12}\}$ species maintained the optical properties of those in solution—showing strong absorptions in both UV and NIR region. Therefore, the $\{\text{Ta}_6\text{Br}_{12}\}@\text{SiO}_2$ nanoparticles we synthesized in this study are promising for the filtration of the most energetic UV-NIR radiations or biotechnology applications. More generally, this work paves the way to the preparation of inorganic nanocomposites powders based on Ta_6 metal clusters.

Declarations

Author contribution statement

Wanghui Chen: Conceived and designed the experiments; Performed the experiments; Analyzed and interpreted the data; Contributed reagents, materials, analysis tools or data; Wrote the paper.

Fabien Grasset: Conceived and designed the experiments; Contributed reagents, materials, analysis tools or data.

Maxence Wilmet, Thai Giang Truong, Noée Dumait, Stéphane Cordier, Yoshio Matsui, Toru Hara, Toshiaki Takei, Norio Saito, Thi Kim Ngan Nguyen, Takeo Oh-sawa, Naoki Ohashi, Tetsuo Uchikoshi: Contributed reagents, materials, analysis tools or data.

Funding statement

This work was supported by Saint-Gobain (France), CNRS, Université de Rennes 1, and NIMS through the Laboratory for Innovative Key Materials and Structures (LINK UMI 3629).

Competing interest statement

The authors declare no conflict of interest.

Additional information

No additional information is available for this paper.

Acknowledgements

This work was carried out as part of the France-Japan international collaboration framework (UMI 3629-LINK Center). The authors wish to thank the people involved in LINK and related activities, particularly David Lechevalier and Dr. Mari Kono of Saint-Gobain KK (Tokyo, Japan).

References

- [1] J. Lowe, D. Stock, B. Jap, P. Zwickl, W. Baumeister, R. Huber, Crystal structure of the 20S proteasome from the archaeon *T. acidophilum* at 3.4 Å resolution, *Science* 268 (1995) 533–539.
- [2] P. Cramer, D.A. Bushnell, J. Fu, A.L. Gnatt, B. Maier-Davis, N.E. Thompson, R.R. Burgess, A.M. Edwards, P.R. David, R.D. Kornberg, Architecture of RNA polymerase II and implications for the transcription mechanism, *Science* 288 (2000) 640–649.
- [3] K.N. Ferreira, T.M. Iverson, K. Maghlaoui, J. Barber, Architecture of the photosynthetic oxygen-evolving center, *Science* 43 (2004) 1831–1839.
- [4] B.F. Mullan, M.T. Madsen, L. Messerle, V. Kolesnichenko, J. Kruger, X-ray attenuation coefficients of high-atomic-number, hexanuclear transition metal cluster compounds: a new paradigm for radiographic contrast agents, *Acad. Radiol.* 7 (2000) 254–259.

- [5] A. Renaud, M. Wilmet, T.G. Truong, M. Seze, P. Lemoine, N. Dumait, W. Chen, N. Saito, T. Ohsawa, T. Uchikoshi, N. Ohashi, S. Cordier, F. Grasset, Transparent tantalum cluster-based UV and IR blocking electrochromic devices, *J. Mater. Chem. C* 5 (2017) 8160–8168.
- [6] N.T. Nguyen, A. Renaud, M. Wilmet, N. Dumait, S. Paofai, D. Benjamin, W. Chen, N. Ohashi, S. Cordier, F. Grasset, T. Uchikoshi, New ultra-violet and near-infrared blocking filters for saving energy applications: fabrication of tantalum metal atom cluster-based nanocomposite thin films by electrophoretic deposition, *J. Mater. Chem. C* 5 (2017) 10477–10484.
- [7] E.J. Welch, J.R. Long, *Atomlike Building Units of Adjustable Character: Solid-state and Solution Routes to Manipulating Hexanuclear Transition Metal Chalcogenide Clusters*, John Wiley & Sons, NJ, 2005.
- [8] B. Perić, D. Jozić, P. Planinić, N. Brničević, G. Giester, Synthesis, crystal structure, spectroscopic and thermal properties of $[\text{Et}_4\text{N}][\text{Ta}_6\text{Br}_{12}(\text{H}_2\text{O})_6]\text{Br}_4 \cdot 4\text{H}_2\text{O}$ (Et=ethyl)-a new compound with the paramagnetic $[\text{Ta}_6\text{Br}_{12}]^{3+}$ cluster core, *J. Solid State Chem.* 182 (2009) 2443–2450.
- [9] F. Ogliaro, S. Cordier, J.-F. Halet, C. Perrin, J.-Y. Saillard, M. Sergent, Detailed structural and theoretical studies of the bonding in edge-bridged halide and oxyhalide octahedral niobium and tantalum clusters, *Inorg. Chem.* 37 (1998) 6199–6207.
- [10] T.G. Gray, Hexanuclear and higher nuclearity clusters of the groups 4-7 metals with stabilizing π -donor ligands, *Coord. Chem. Rev.* 243 (2003) 213–235.
- [11] D. Bauer, H.-G. Schnering, Beiträge zur Chemie der Elemente Niob und Tantal. LXVII. Die Struktur der Tantalhalogenide $\text{Ta}_6\text{Cl}_{15}$ und $\text{Ta}_6\text{Br}_{15}$, *Z. Anorg. Allg. Chem.* 361 (1968) 259–276.
- [12] F.W. Koknat, J.A. Parsons, A. Vongvusharintra, Metal cluster halide complexes. i. efficient synthesis of hydrated hexanuclear niobium and tantalum cluster halides $\text{M}_6\text{X}_{14} \cdot 8\text{H}_2\text{O}$, *Inorg. Chem.* 13 (1974) 1699–1702.
- [13] D.N.T. Hay, L. Messerle, Low-temperature, high yield synthesis, and convenient isolation of the high-electron-density cluster compound $\text{Ta}_6\text{Br}_{14} \cdot 8\text{H}_2\text{O}$ for use in biomacromolecular crystallographic phase determination, *J. Struct. Biol.* 139 (2002) 147–151.
- [14] B.G. Hughes, J.L. Meyer, P.B. Fleming, R.E. Mccarley, Chemistry of polynuclear metal halides. III. synthesis of some niobium and tantalum $\text{m}_6\text{X}_{12}^{n+}$ cluster derivatives, *Inorg. Chem.* 9 (1970) 1343–1346.

- [15] P.A. Vaughan, J.H. Sturdivant, L. Pauling, The determination of the structures of complex molecules and ions from X-ray diffraction by their solutions: the structures of the groups PtBr_6^- , PtCl_6^- , $\text{Nb}_6\text{Cl}_{12}^{++}$, $\text{Ta}_6\text{Br}_{12}^{++}$, and $\text{Ta}_6\text{Cl}_{12}^{++}$, *J. Am. Chem. Soc.* 72 (1950) 5477–5486.
- [16] N. Prokopuk, D.F. Shriver, The octahedral M_6Y_8 and M_6Y_{12} clusters of group 4 and 5 transition metals, *Adv. Inorg. Chem.* 46 (1998) 1–49.
- [17] Š.M.N. Brničević, Cluster hydroxides of the composition $\text{M}_2[\text{Ta}_6\text{Cl}_{12}](\text{OH})_6 n\text{H}_2\text{O}$ with $\text{M}=\text{Na}, \text{K}, \text{Rb}, (\text{CH}_3)_4\text{N}^+$ and $(\text{C}_2\text{H}_5)_4\text{N}^+$ air oxidation of the cluster unit $[\text{Ta}_6\text{Cl}_{12}]^{2+}$ in alkaline medium, *Croat. Chem. Acta* 57 (1984) 529–535.
- [18] A. Kashta, N. Brničević, R.E. Mccarley, Reactions of niobium and tantalum clusters with aliphatic alcohols. Synthesis and properties of $[\text{M}_6\text{X}_{12}(\text{ROH})_6]\text{X}_2$, $\text{M} = \text{Nb}$ or Ta , $\text{X} = \text{Cl}$ or Br , $\text{R} = \text{Me}, \text{Et}, i\text{-Pr}$ or $i\text{-Bu}$, *Polyhedron* 10 (1991) 2031–2036.
- [19] M.N. Sokolov, P.A. Abramov, M.A. Mikhailov, E.V. Peresypkina, A.V. Virovets, V.P. Fedin, Simplified synthesis and structural study of $\{\text{Ta}_6\text{Br}_{12}\}$ clusters, *Z. Anorg. Allg. Chem.* 636 (2010) 1543–1548.
- [20] M.B. Robin, N.A. Kuebler, Color and nonintegral valence in niobium and tantalum subhalides, *Inorg. Chem.* 4 (1965) 978–985.
- [21] B. Spreckelmeyer, Absorptionsspektren von Verbindungen mit $[\text{Nb}_6\text{X}_{12}]$ - und $[\text{Ta}_6\text{X}_{12}]$ -gruppen ($\text{X} = \text{Halogen}$), *Z. Anorg. Allg. Chem.* 365 (1969) 225–242.
- [22] P.B. Fleming, J.L. Meyer, W.K. Grindstaff, R.E. McCarley, Chemistry of polynuclear metal halides. VIII. Infrared spectra of some $\text{Nb}_6\text{X}_{12}^{n+}$ and $\text{Ta}_6\text{X}_{12}^{n+}$ derivatives, *Inorg. Chem.* 9 (1970) 1769–1771.
- [23] K. Osseo-Asare, F.J. Arriagada, Preparation of SiO_2 nanoparticles in a non-ionic reverse micellar system, *Colloids Surf* 50 (1990) 321–339.
- [24] C.-L. Chang, H.S. Fogler, Kinetics of silica particle formation in nonionic W/O microemulsions from TEOS, *Mater. Interfaces Electrochem. Phenom.* 42 (1996) 3153–3163.
- [25] K.S. Finnie, J.R. Bartlett, C.J.A. Barbé, L. Kong, Formation of silica nanoparticles in microemulsions, *Langmuir* 23 (2007) 3017–3024.
- [26] S.Y. Chang, L. Liu, S.A. Asher, Preparation and properties of tailored morphology, monodisperse colloidal silica-cadmium sulfide nanocomposites, *J. Am. Chem. Soc.* 116 (1994) 6739–6744.

- [27] T. Aubert, F. Grasset, S. Mornet, E. Duguet, O. Cador, S. Cordier, Y. Molard, V. Demange, M. Mortier, H. Haneda, Functional silica nanoparticles synthesized by water-in-oil microemulsion processes, *J. Colloid Interface Sci.* 341 (2010) 201–208.
- [28] A. Guerrero-Martínez, J. Pérez-Juste, L.M. Liz-Marzán, Recent progress on silica coating of nanoparticles and related nanomaterials, *Adv. Mater.* 22 (2010) 1182–1195.
- [29] J. Wang, Z.H. Shah, S. Zhang, R. Lu, Silica-based nanocomposites via reverse microemulsions: classifications, preparations, and applications, *Nanoscale* 6 (2014) 4418.
- [30] A.K. Ganguli, T. Ahmad, S. Vaidya, J. Ahmed, Microemulsion route to the synthesis of nanoparticles, *Pure Appl. Chem.* 80 (2008) 2451–2477.
- [31] T. Ahmad, A.K. Ganguli, Structural and dielectric characterization of nanocrystalline (Ba, Pb)ZrO₃ developed by reverse micellar synthesis, *J. Am. Ceram. Soc.* 89 (2006) 3140–3146.
- [32] T. Ahmad, K. Ramanujachary, S.E. Lofland, A.K. Ganguli, Reverse micellar synthesis and properties of nanocrystalline GMR materials (LaMnO₃, La_{0.67}Sr_{0.33}MnO₃ and La_{0.67}Ca_{0.33}MnO₃): ramifications of size, *J. Chem. Sci.* 118 (2006) 513–518.
- [33] R. Koole, M.M. Van Schooneveld, J. Hilhorst, C.D.M. Donegá, C. Hart, A. Van Blaaderen, D. Vanmaekelbergh, A. Meijerink, D.C. Hart, On the incorporation mechanism of hydrophobic quantum dots in silica spheres by a reverse microemulsion method on the incorporation mechanism of hydrophobic quantum dots in silica spheres by a reverse microemulsion method, *Chem. Mater.* 20 (2008) 2503–2512.
- [34] Y. Zhu, F.Y. Jiang, K. Chen, F. Kang, Z.K. Tang, Modified reverse microemulsion synthesis for iron oxide/silica core-shell colloidal particles, *J. Sol. Gel Sci. Technol.* 66 (2013) 180–186.
- [35] F. Grasset, N. Labhsetwar, D. Li, D.C. Park, N. Saito, H. Haneda, O. Cador, T. Roisnel, S. Mornet, E. Duguet, J. Portier, J. Etourneau, Synthesis and magnetic characterization of zinc ferrite nanoparticles with different environments: powder, colloidal solution, and zinc ferrite-silica core-shell nanoparticles, *Langmuir* 18 (2002) 8209–8216.
- [36] F. Grasset, R. Marchand, A.M. Marie, D. Fauchadour, F. Fajardie, Synthesis of CeO₂@SiO₂ core-shell nanoparticles by water-in-oil microemulsion. Preparation of functional thin film, *J. Colloid Interface Sci.* 299 (2006) 726–732.

- [37] J.H. Son, H.Y. Park, D.P. Kang, D.S. Bae, Synthesis and characterization of Ag/Pd doped SiO₂ nanoparticles by a reverse micelle and sol-gel processing, *Colloids Surf. A* 313–314 (2008) 105–107.
- [38] J. Qian, Z. Zhou, X. Cao, S. Liu Songqin, Electrochemiluminescence immunosensor for ultrasensitive detection of biomarker using Ru(bpy)₃²⁺-encapsulated silica nanosphere labels, *Anal. Chim. Acta* 665 (2010) 32–38.
- [39] H.L. Ding, Y.X. Zhang, S. Wang, J.M. Xu, S.C. Xu, G.H. Li, Fe₃O₄@SiO₂ core/shell nanoparticles: the silica coating regulations with a single core for different core sizes and shell thicknesses, *Chem. Mater.* 24 (2012) 4572–4580.
- [40] F. Grasset, F. Dorson, S. Cordier, Y. Molard, C. Perrin, A.-M. Marie, T. Sasaki, H. Haneda, Y. Bando, M. Mortier, Water-in-oil microemulsion preparation and characterization of Cs₂[Mo₆X₁₄]@SiO₂ phosphor nanoparticles based on transition metal clusters (X = Cl, Br, and I), *Adv. Mater.* 20 (2008) 143–148.
- [41] T. Aubert, F. Cabello-Hurtado, M.A. Esnault, C. Neaime, D. Leuret-Chauvel, S. Jeanne, P. Pellen, C. Roiland, L. Le Polles, N. Saito, K. Kimoto, H. Haneda, N. Ohashi, F. Grasset, S. Cordier, Extended investigations on luminescent Cs₂[Mo₆Br₁₄]@SiO₂ nanoparticles: physico-structural characterizations and toxicity studies, *J. Phys. Chem. C* 117 (2013) 20154–20163.
- [42] Y.A. Vorotnikov, O.A. Efremova, N.A. Vorotnikova, K.A. Brylev, M.V. Edeleva, A.R. Tsygankova, A.I. Smolentsev, N. Kitamura, Y.V. Mironov, M.A. Shestopalov, On the synthesis and characterisation of luminescent hybrid particles: Mo₆ metal cluster complex/SiO₂, *RSC Adv.* 6 (2016) 43367–43375.
- [43] C. Neaime, M. Amela-Cortes, F. Grasset, Y. Molard, S. Cordier, B. Dierre, M. Mortier, T. Takei, K. Takahashi, H. Haneda, M. Verelst, S. Lechevallier, Time-gated luminescence bioimaging with new luminescent nanocolloids based on [Mo₆I₈(C₂F₅COO)₆]²⁻ metal atom clusters, *Phys. Chem. Chem. Phys.* 18 (2016) 30166–30173.
- [44] A.O. Solovieva, Y.A. Vorotnikov, K.E. Trifonova, O.A. Efremova, A.A. Krasilnikova, K.A. Brylev, E.V. Vorontsova, P.A. Avrorov, L.V. Shestopalova, A.F. Poveshchenko, Y.V. Mironov, M.A. Shestopalov, Cellular internalisation, bioimaging and dark and photodynamic cytotoxicity of silica nanoparticles doped by {Mo₆I₈}⁴⁺ metal clusters, *J. Mater. Chem. B* 4 (2016) 4839–4846.

- [45] N. Brničević, H. Schüfer, Die reaktion der komplexe $[M_6X_{12}]X_2 \cdot 8H_2O$ ($M = Nb, Ta; X = Cl, Br$) mit natronlauge, *Z. Anorg. Allg. Chem.* 441 (1978) 219–229.
- [46] P.J. Kuhn, R.E. Mccarley, Chemistry of polynuclear metal halides. I. preparation of the polynuclear tantalum halides Ta_6X_{14} , *Inorg. Chem.* 4 (1965) 1482–1486.
- [47] B. Spreckelmeyer, Beiträge zur chemie der elemente niob und tantal. LXVI. wasserhaltige verbindungen mit $[Me_6X_{12}]$ -gruppen ($Me = Nb, Ta; X = Cl, Br$), *Z. Anorg. Allg. Chem.* 358 (1968) 147–162.
- [48] S.A. Best, R.A. Walton, X-ray photoelectron spectra of inorganic molecules. 22. Halogen core electron binding energies of low oxidation state molybdenum bromide and molybdenum iodide clusters and niobium and tantalum chlorides containing the $[M_6Cl_{12}]^{n+}$ cores, *Inorg. Chem.* 18 (1979) 484–488.
- [49] B. Spreckelmeyer, H. Schäfer, Die photometrische titration des $[Ta_6Br_{12}]^{2+}$ -Ions, *J. Less Common Met.* 13 (1967) 127–129.